Tidal deformability doppelgänger: Implications of a low-density phase transition in the neutron star equation of state

Carolyn A. Raithel[1,*] and Elias R. Most[2,†]

[1]*School of Natural Sciences, Institute for Advanced Study, 1 Einstein Drive, Princeton, New Jersey 08540, USA; Princeton Center for Theoretical Science, Jadwin Hall, Princeton University, Princeton, New Jersey 08544, USA; and Princeton Gravity Initiative, Jadwin Hall, Princeton University, Princeton, New Jersey 08544, USA*

[2]*TAPIR 350-17, California Institute of Technology, 1200 E California Boulevard, Pasadena, California 91125 USA*

(Received 8 August 2022; accepted 19 June 2023; published 11 July 2023)

Studying the properties of ultradense matter is one of the key goals of modern neutron star research. The measurement of the tidal deformability from the inspiral of a binary neutron star merger offers one promising method for constraining the equation of state (EoS) of cold, dense matter. In this work, we report on a new class of EoSs which have significantly different pressures at nuclear densities and large differences in stellar radii, but that predict surprisingly similar tidal deformabilities across the entire range of astrophysically-observed neutron star masses. Using a survey of 5 million piecewise polytropic EoSs, subject to five different sets of nuclear priors, we demonstrate that these "tidal deformability doppelgängers" occur generically. We find that they can differ substantially in the pressure (by up to a factor of 3 at nuclear densities) and in the radius of intermediate-mass neutron stars (by up to 0.5 km), but are observationally indistinguishable in their tidal deformabilities ($\Delta\Lambda \lesssim 30$) with the sensitivity of current gravitational wave detectors. We demonstrate that this near-degeneracy in the tidal deformability is a result of allowing for a phase transition at low densities. We show that a combination of input from nuclear theory (e.g., from chiral effective field theory), x-ray observations of neutron star radii, and/or the next generation of gravitational wave detectors will be able to significantly constrain these tidal deformability doppelgängers.

DOI: 10.1103/PhysRevD.108.023010

I. INTRODUCTION

Astrophysical observations of neutron stars provide a unique laboratory for constraining the equation of state (EoS) of ultra-dense matter. Such constraints have been made, for example, using measurements of the neutron star radius from spectral modeling of bursting or quiescent neutron stars in x-ray binaries [1–9] or, more recently, from pulse-profile modeling of x-ray pulsars with the Neutron star Interior Composition ExploreR (NICER) [10–13]. With the advent of gravitational wave (GW) astronomy, a complementary avenue for constraining the EoS is now also possible.

In particular, observations of the inspiral gravitational waves from the first binary neutron star merger, GW170817, have constrained the tidal deformability of a $1.4M_\odot$ star to $\Lambda_{1.4} = 190^{+390}_{-120}$ at 90% confidence, which in turn has been used to constrain the pressure at twice the nuclear saturation density to within ∼125% [14–16]. It is projected that within the next five years, the LIGO-Virgo-Kagra network is likely to detect $\mathcal{O}(10\text{–}20)$ additional neutron star mergers with high signal-to-noise ratios (SNRs), which could further constrain the pressure at twice nuclear densities to within a factor of ∼2 [17–20]; or, potentially to within 20% given certain assumptions about the nuclear EoS [21].

With the construction of next-generation GW detectors such as Cosmic Explorer [22], Einstein Telescope [23], or NEMO [24], even tighter constraints on the EoS will become possible in the 2030s. For example, an event like GW170817 would have an SNR of 2800 with Cosmic Explorer, roughly 88 times larger than was observed in 2017 [25]. These detectors will observe tens of thousands of events per year, hundreds of which will have extremely high SNR in the inspiral, leading to anticipated constraints on the binary tidal deformability of $\sigma_{\tilde{\Lambda}} < 20$ and thus enabling a new era of precision EoS constraints [26].

The prospects for constraining the EoS with current or next-generation GW observations relies on the unique mapping between the tidal deformability and the

*craithel@ias.edu
†emost@caltech.edu

underlying EoS. In the standard paradigm, these constraints would be limited only by the sensitivity to which the tidal deformability can be measured, and the masses at which it is measured. In practice, effects such as dynamical tides [27,28] or systematics in the available waveform models [29] may complicate the extraction of the tidal deformability from the inspiral GWs, but the tidal deformability itself is assumed to map robustly to the EoS at supranuclear densities.

In this paper, we describe a new construction of EoS models that poses a challenge to this paradigm. In particular, we demonstrate that uncertainties in the EoS above nuclear densities lead to the emergence of what we call "tidal deformability doppelgängers"; these are EoS models that differ significantly in pressure at supranuclear densities and accordingly in the neutron star radius, but that predict nearly identical tidal deformabilities across a wide range of neutron star masses. The most extreme of these doppelgänger EoSs can vary in the pressure by factors of $\sim$3 and in the radius by up to 0.5 km, but they differ in the tidal deformability by $\lesssim$10 across the entire range of astrophysically-observed neutron star masses, making them observationally indistinguishable to current GW detectors.

We find that pairs of doppelgänger EoSs are ubiquitous in randomly-generated EoS samples and that they occur as a natural consequence of allowing for a phase transition in the EoS at densities between 1 and 2 times the nuclear saturation density (where the exact density depends on the details of the crust EoS and the high-density parametrization, as we will demonstrate). We demonstrate that these doppelgängers can be constructed by exploiting the different density dependencies of the tidal Love number, k_2, and the stellar compactness, C, such that the tidal deformability $\Lambda = (2/3)k_2 C^{-5}$ remains the same, in spite of large differences in the stellar radii and pressures at supranuclear densities. Interestingly, we find that the doppelgängers approximately obey the quasiuniversal relations between the tidal deformability and the moment of inertia, but that the doppelgängers tend to fall below the standard quasiuniversal relations with stellar compactness [30].

The small differences in the tidal deformability curves of the doppelgänger models will likely require the next generation of GW detectors to resolve. We demonstrate, however, that the parameter space that is subject to this tidal deformability degeneracy can also be reduced by applying more restrictive nuclear priors, e.g., on the crust EoS or on the density derivatives of the pressure. At low densities, such constraints may come from nuclear theory (e.g., from chiral EFT [31–34]); while new measurements of neutron star radii or even broad constraints on the tidal deformability with current GW detectors may also help to constrain the parameter space of the tidal deformability doppelgängers, even before the advent of next-generation detectors.

The outline of the paper is as follows. In Sec. II, we introduce several examples of doppelgänger EoSs and illustrate their basic construction. In Sec. III, we perform a large-scale EoS parameter survey with different sets of nuclear priors, to characterize the regions of EoS parameter space where the tidal deformability degeneracy can occur and we quantify the unique signatures of these models. In Sec. IV, we discuss the implications of the doppelgänger EoSs and the prospects for resolving the degeneracy with joint input from nuclear physics and astrophysics.

II. OBSERVATIONAL DEGENERACY BETWEEN EOS MODELS WITH LOW-DENSITY PHASE TRANSITIONS

We start in this section by introducing a few examples of tidal deformability doppelgängers, in order to illustrate their key features.

Here and throughout this paper, we utilize parametric models of the EoS to explore the EoS parameter space in search of doppelgänger models. In particular, we adopt a piecewise polytropic (PWP) parametrization of the EoS, using five polytropic segments that are spaced uniformly in the logarithm of the density between ρ_0 and $7.4\rho_{\rm sat}$ [35–37], where $\rho_{\rm sat} = 2.7 \times 10^{14}$ g/cm^3 is the nuclear saturation density. The starting density of the parametrization is taken to be between $\rho_{\rm sat}$ and $1.5\rho_{\rm sat}$, below which we adopt a tabular, nuclear EoS to describe the crust. For these crust EoSs, we choose nuclear models that are consistent with low-density nuclear constraints. We fix the pressure at ρ_0 to that of the crust EoS, in order to ensure continuity in the resulting model. The five polytropic segments of the PWP EoS are then determined by specifying the pressures at each fiducial density in the model.

In constructing new EoSs, we impose a set of minimal physical constraints on the EoS above ρ_0, namely that:

(1) The EoS must be hydrostatically stable (i.e., $\partial P/\partial\rho \geq 0$, where P is the pressure and ρ is the rest-mass density).
(2) The sound speed must remain subluminal at all densities.
(3) The EoS must be consistent with the observation of massive pulsars. In particular, we require that $M_{\rm max} > 2.01 M_\odot$, which corresponds to the 1σ lower limit on the current most massive neutron star [38,39].

Once these minimal constraints are satisfied, we exploit the uncertainties in the EoS to freely explore the remaining parameter space. We note that the resulting EoSs are quite broad in their coverage. We intentionally explore the extremes of the EoS parameter space in order to identify and highlight the new behavior of the doppelgänger models. As we will demonstrate, by applying additional nuclear input, the ubiquity and extremity of the doppelgängers can be significantly reduced.

We introduce the concept of tidal deformability doppelgängers with a few examples in Fig. 1. In this first illustration, we have chosen commonly used low-density EoSs, onto which we attach different high-density EoSs

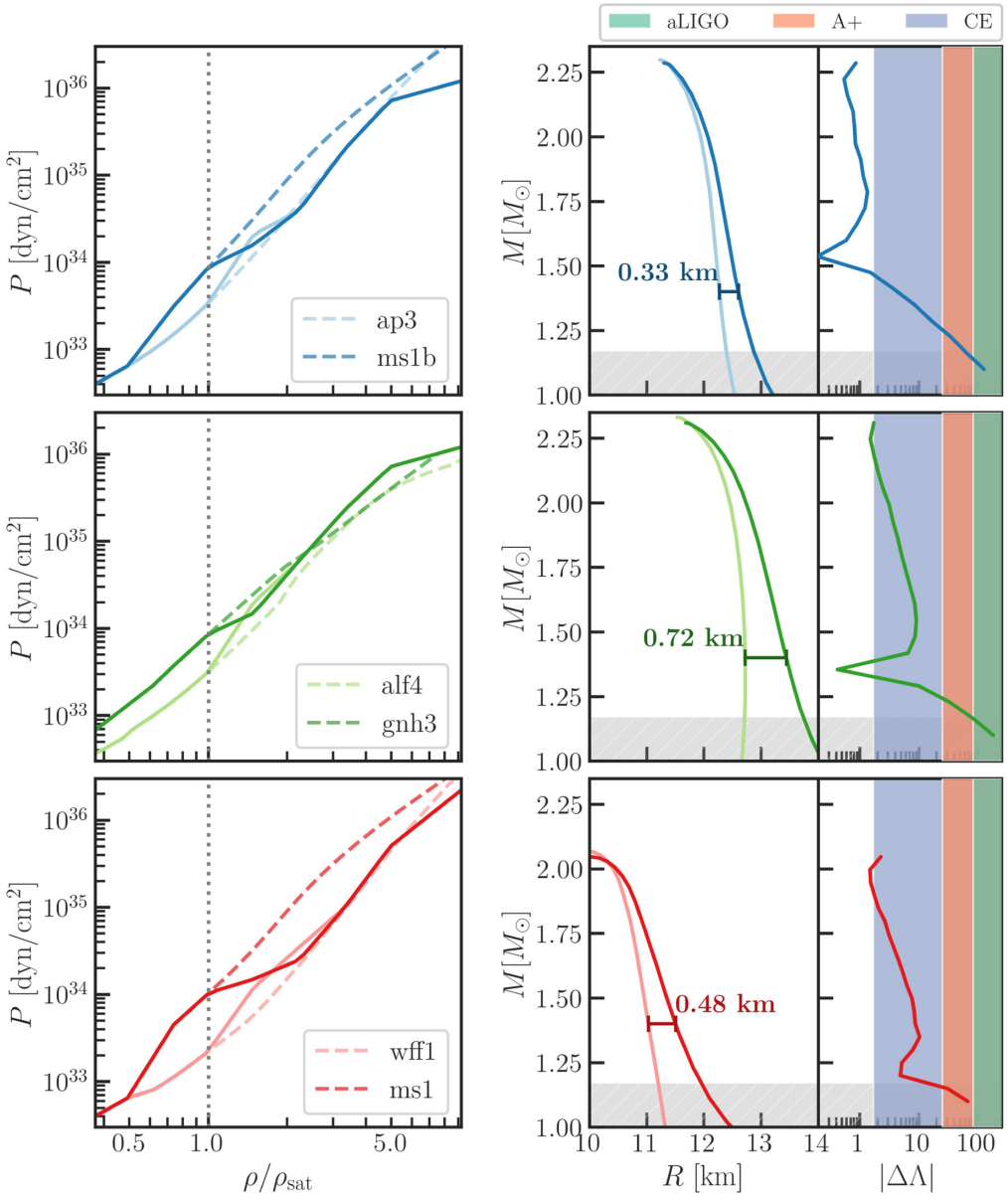

FIG. 1. Three example pairs of doppelgängers, each constructed by assuming a different microphysical EoS for the crust. The various crust EoSs (which are shown with dashed lines) are used up to $\rho_{\rm sat}$; at higher densities, we use piecewise polytropes to explore the parameter space and to illustrate the degeneracy in tidal deformabilities. The EoSs are shown in the left column; the middle column shows the corresponding mass-radius relations; and the right column shows the absolute difference in tidal deformability at each mass, for a given pair of doppelgängers. The vertical bands indicate the expected 68% measurement uncertainty in the tidal deformability for a population of neutron star mergers, assuming an intermediate merger detection rate, for the sensitivity of LIGO at design sensitivity (aLIGO), the anticipated sensitivity of LIGO during its fifth observing run (A+), and the proposed XG detector Cosmic Explorer (CE) [25]. Masses below the lightest-observed neutron star mass are masked in gray.

that are constructed using PWPs to produce similar tidal deformability curves. For example, in the top row of Fig. 1, the light blue model uses the variational-method nuclear EoS ap3 [40] to describe the crust up to $\rho_{\rm sat}$; while the dark blue model uses the relativistic mean-field EoS ms1b [41] for the crust. At $\rho > \rho_{\rm sat}$, we switch to the PWP construction described above, and we adjust the high-density pressures to specifically minimize differences in the tidal deformability Λ. The net result is a pair of EoSs that differ in the pressure at $\rho_{\rm sat}$ by a factor of 2.6, in the radius $R_{1.4}$ of a $1.4M_\odot$ star by 0.33 km, but differ by $\Delta\Lambda \lesssim 10$ across the entire range of astrophysically observed neutron star masses. The second and third rows of Fig. 1 show two additional pairs of doppelgänger EoSs, which are constructed using different sets of crust EoSs: gnh3 [42], alf4 [43], wff1 [44], and ms1, which is identical to ms1b but

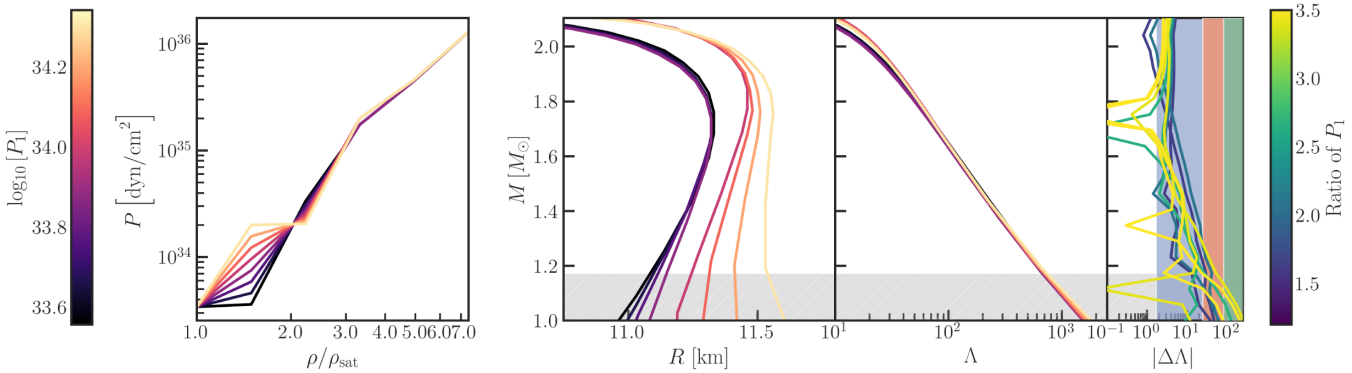

FIG. 2. Tidal deformability degeneracy for an example family of doppelgänger EoSs. From left to right, we show the EoS pressure as a function of density, the mass-radius ($M-R$) relation for each EoS, and the mass-tidal deformability relation. The curves in these first three figures are colored according to the EoS pressure at the first fiducial density, $1.5\rho_{\mathrm{sat}}$, where ρ_{sat} is the nuclear saturation density. The figure on the far right shows the absolute difference in Λ between any two of these EoSs, with a blue-green color scale to indicate the ratio of pressures at ρ_{sat} for the two EoSs being compared. The vertical shaded bands indicate the expected detection sensitivity in Λ for a population of mergers observed with current and next-generation detectors, and masses below the lightest-observed neutron star mass are masked in gray (as in Fig. 1). For any pair EoSs, the tidal deformabilities differ by $\lesssim 50$ across the entire range of astrophysical neutron star masses, even though the pressures at $1.5\rho_{\mathrm{sat}}$ differ by a factor of 5.

features a higher symmetry energy (for additional details on these models, see e.g., [45]). In Fig. 1, we have grayed out masses below $1.17M_\odot$, which is the 1-σ lower limit on the lightest-observed pulsar [46], in order to focus on astrophysically observed neutron star masses.[1] In these examples, we find fractional differences in pressure of 170% and in $R_{1.4}$ of 0.72 km for the gnh3/alf4 pair of doppelgängers (in green); and 365% in pressure and 0.48 km in $R_{1.4}$ for the wff1/ms1 pair of doppelgängers (in red).

Despite these large differences in pressure and radius, the tidal deformabilities for each set of models are very similar in all three cases. We show the difference in tidal deformability as a function of the mass for each pair of models in the far right column of Fig. 1. In these figures, the vertical shaded bands indicate anticipated 68% measurement uncertainties in the tidal deformability, σ_Λ, for a population of neutron star mergers, assuming an intermediate merger detection rate observed with current and next-generation facilities [25].[2] When this measurement uncertainty, σ_Λ, becomes comparable to the intrinsic difference between a pair of models, $\Delta\Lambda$, the two EoSs can no longer be distinguished. Already, we see that a next-generation detector such as Cosmic Explorer would be required to distinguish between any of these pairs of doppelgängers based on their tidal deformabilities alone.

We note that we focus on absolute differences in radii and tidal deformabilities, because this allows for the most direct comparison against the observational sensitivity of experiments such as NICER or LIGO. For example, it has been estimated that the sensitivity of next-generation GW detectors will yield constraints on the neutron star radii of 50–200 m [26], significantly smaller than what we construct for the doppelgänger models shown in Fig. 1. To explore the impact of this tidal deformability degeneracy for current and future GW detector sensitivities, we perform mock Bayesian inferences of the EoS for a pair of doppelgänger models in a companion paper [47].

The examples shown here were constructed by using different theoretical calculations for the crust EoS up to ρ_{sat} and freely varying the PWP pressures at higher densities. These results are consistent with previous work that has shown that changing the crust EoS (at densities below 10^{14} g/cm^3) can affect the radius without significantly changing the tidal deformabilities [48]. Here, however, we find that EoSs can have significant ($\sim 3\times$) differences at *supranuclear* densities, and still be indistinguishable in their tidal deformabilities.

We can also see this behavior emerge more generically, by systematically varying the EoS at densities above ρ_{sat} to explore the uncertainties in the EoS at supranuclear densities. We do so in Fig. 2, where we adopt a single low-density EoS, ap3, which we use at densities below ρ_{sat} for all models. At densities above ρ_{sat}, we construct a sequence of models that exhibit similar tidal deformability curves as the supranuclear pressures are varied.

In Fig. 2, it becomes clear that there is actually a continuum of EoS models that produce nearly degenerate tidal deformability curves. The mass-radius and tidal deformability curves for these models are shown in the

[1]We note that the 90% lower limit on the secondary mass from GW170817 was also $1.17M_\odot$ and that, to date, no lighter neutron stars have yet been detected from gravitational wave events [14].

[2]We note that the σ_Λ from [25] was calculated for the binary tidal deformability, $\tilde{\Lambda}$. In this paper, we assume equal mass binaries for simplicity, in which case $\tilde{\Lambda}$ reduces to the tidal deformability of either star. We present the difference in $\tilde{\Lambda}$ as a function of the mass ratio for two example pairs of doppelgänger EoSs in a companion paper [47].

middle panels of Fig. 2, where they are colored according to the pressure at the nuclear saturation density, $P_{\rm sat}$. The far right panel of Fig. 2 shows the difference in tidal deformability between any two pairs of these EoSs, colored according to the ratio of pressures at $1.5\rho_{\rm sat}$. As we saw in Fig. 1, the tidal deformabilities of these models are nearly indistinguishable with current GW detectors for all but the lowest-mass systems. In this case, the doppelgängers would be distinguishable in an EoS inference from GW data only by the choice of informative nuclear priors. In contrast, for a population of mergers observed with Cosmic Explorer, these models start to become distinguishable from the data directly.

The fact that the near-degeneracy in tidal deformability curves applies to a continuous range of EoS parameter space has important implications: it suggests that even as the range of EoS pressures is further constrained by future astrophysical detections and by input from nuclear theory, the tidal deformability degeneracy will be reduced, but not entirely eliminated. We revisit this point and discuss practical ways for further resolving the degeneracy in Sec. IV.

III. EOS PARAMETER SURVEY

Having now introduced the common features of a few examples of tidal deformability doppelgängers, in this section, we turn to a large-scale parameter survey, in order to illustrate the ubiquity of the doppelgänger EoSs and to quantify the specific regions of parameter space that are susceptible to this tidal deformability degeneracy.

A. Construction of parameteric EoSs

To that end, we construct five samples of piecewise polytropic EoSs. All EoSs consist of five polytropic segments, as described in Sec. II. We consider three fiducial densities for the onset of our piecewise polytopes, $\rho_0 = \{1, 1.2, \text{ and } 1.5\}\rho_{\rm sat}$, in order to gauge the impact of this starting density on the doppelgänger behavior. At densities below this fiducial value, we adopt a tabulated, nuclear EoS to describe the crust. The pressure at ρ_0 is set by the crust EoS, in order to ensure continuity in the EoS. We explore two choices for the crust EoS. For the baseline set of models, we use the nuclear model ap3 [40] for the crust; but we also explore the impact of one stiffer EoS model, ms1b [41], which predicts a significantly (2.6×) larger pressure at $\rho_{\rm sat}$ (see top panel of Fig. 1).

The pressures at the remaining five fiducial densities are free parameters, which we sample uniformly via a Markov-chain Monte Carlo (MCMC). A tentative MCMC step is rejected if it violates any of the minimal constraints enumerated in Sec. II. We additionally impose a regularizer on the pressure in our MCMC sampling, in order to penalize EoS models that have extreme density variations in the pressure. This helps to compensate for the large degree of freedom inherent to a five-polytrope EoS.

TABLE I. Overview of EoS populations considered in this work.

Starting density	Crust EoS	Prior choice
$\rho_{\rm sat}$	ap3	Weak ($\lambda = 8$)
$1.2\rho_{\rm sat}$	ap3	Weak ($\lambda = 8$)
$1.5\rho_{\rm sat}$	ap3	Weak ($\lambda = 8$)
$\rho_{\rm sat}$	ms1b	Weak ($\lambda = 8$)
$\rho_{\rm sat}$	ap3	Strong ($\lambda = 2$)

We construct the regularizer to be a Gaussian over the second logarithmic derivative of the pressure, i.e.,

$$\xi = \exp\left[-\frac{(d^2(\ln P)/d(\ln\rho)^2)^2}{2\lambda^2}\right], \tag{1}$$

where λ is the characteristic scale. The distribution of $d^2(\ln P)/d(\ln\rho)^2$ evaluated at different densities for a large sample of theoretical EoSs is shown in Fig. 1 of [49]. Based on those results, we adopt a conservative value of $\lambda = 8$ for our baseline models, which corresponds to a weakly informative prior. We also construct one set of models with $\lambda = 2$, which corresponds to taking stronger (more informative) input from the existing set of nuclear models. For further details about how the choice of this Gaussian regularizer affects an EoS inference, see [49].

Altogether, we construct five different sets of PWP EoSs; our baseline model starts at $\rho_{\rm sat}$, uses ap3 for the crust EoS, and adopts a weak prior on the second derivative of the pressures. We explore two samples with the same crust and prior, but starting the PWP parametrization at $\rho_0 = 1.2$ and $1.5\rho_{\rm sat}$. We additionally modify the baseline sample to use ms1b for the crust EoS, keeping ρ_0 and the weak prior the same; and to use a stronger prior, keeping ρ_0 and the crust EoS the same. For each case, we generate a large number (2–4 million) of parametric EoSs, in order to densely sample the five-dimensional EoS parameter space. We summarize these samples in Table I for reference in the following analysis.

B. Döppelganger scoring metric

Within each EoS sample described in Table I, we search for models that show minimal differences in their tidal deformability curves, in spite of large differences in the EoS. In particular, we take a subset of $\sim 9 \times 10^5$ models and compare each of these to every other EoS in the full sample. For each possible pair of EoSs, we define a "doppelgänger score" according to

$$\mathcal{D} = \exp\left[-\frac{(\Delta\Lambda_{\rm max})^2}{2\sigma_\Lambda^2}\right]\left\{1 - \exp\left[-\frac{(\Delta R_{\rm min})^2}{2\sigma_R^2}\right]\right\}, \tag{2}$$

where $\Delta\Lambda_{\rm max}$ is defined as the maximum difference (i.e., the L^∞-norm) in Λ between the two EoSs at any mass

across the astrophysically observed mass range, which we take to span from the lightest observed pulsar at $1.17M_\odot$ [46] to $2.01M_\odot$ [38,39], at their 1-σ lower limits. We calculate $\Delta R_{\rm min}$ as the minimum difference in radius between the two EoSs across the same mass range. The first term in Eq. (2) is one for EoSs that predict identical tidal deformabilities at all masses, and goes to zero as the tidal deformability curves become less similar; while the second term is zero for EoSs with identical mass-radius curves, and approaches one as the mass-radius curves become more distinct. Thus, the doppelgänger scoring criteria is largest when $\Delta\Lambda_{\rm max}$ is *minimized* and $\Delta R_{\rm min}$ is *maximized*. Finally, to set the scale in Eq. (2), we define $\sigma_\Lambda = 10$ and $\sigma_R = 0.3$ km, based on the characteristic differences that we found in Λ and R in Sec. II.

We note that this scoring metric necessarily selects for doppelgängers that are similar to what we constructed by hand in Sec. II. Other scoring criteria would select for different features. For example, maximizing a mass-averaged ΔR (instead of $\Delta R_{\rm min}$) tends to select for EoSs that are dominated by large differences in radius near the maximum mass turn-over, even if the mass-radius curves are identical at other masses. It may also be possible to search for doppelgänger behavior directly in pressure-density space. Empirically, we find that the scoring criteria in Eq. (2) works well for identifying doppelgängers with similar phenomenological features to the examples shown in Sec. II.

For each EoS in our $\sim 9 \times 10^5$ subset, we use Eq. (2) to identify a "best" doppelgänger companion out of all possible (2–4 million) companions. For many EoSs, there is no high-scoring doppelgänger companion, and the "best" score is correspondingly very low. However, for the highest-scoring pairs of EoS, we find doppelgängers that are comparable to those constructed by hand in Figs. 1 and 2.

C. Population properties

We compute the distribution of scores $\mathcal{D}$ for each sample of randomly-generated EoSs and we classify as doppelgängers those pairs of EoSs that have $\mathcal{D}$ within 90% of the highest score found. This criterion selects $\mathcal{O}(10^3$–$10^4)$ doppelgängers for each sample of EoSs. We show contours of the mass-averaged $\Delta\Lambda$ and ΔR for these models in Figs. 3–5.

To start, Fig. 3 shows the results for the EoS samples that start their PWP parametrizations at $\rho_0 = \{1, 1.2, \text{ and } 1.5\}\rho_{\rm sat}$. All three of these samples use the same low-density crust EoS (ap3) and the same weak prior (see Table I). For comparison, Fig. 3 also includes contours of the mass-averaged $\Delta\Lambda$ and ΔR for 5,000 randomly drawn pairs of EoSs from each sample in the unfilled contours.

In general, randomly paired EoSs have large differences in tidal deformability, which are correlated with the difference in radius, as one might typically expect. In contrast, the samples of EoSs that we identify as doppelgängers occupy a distinct part of the EoS parameter space. These have average differences in Λ of $\lesssim 10$, indicating that the mass-tidal deformability curves of these pairs of EoSs are extremely similar to one another, while the average difference in radius is $\sim$0.1–0.4 km. From Fig. 3, we already see that the EoS sample constructed with the PWP parametrization starting at $\rho_{\rm sat}$ enables the most extreme set of doppelgängers, with average radius differences of up to $\sim$400 m. As the crust EoS is enforced to higher densities, the allowed doppelgängers become less extreme.

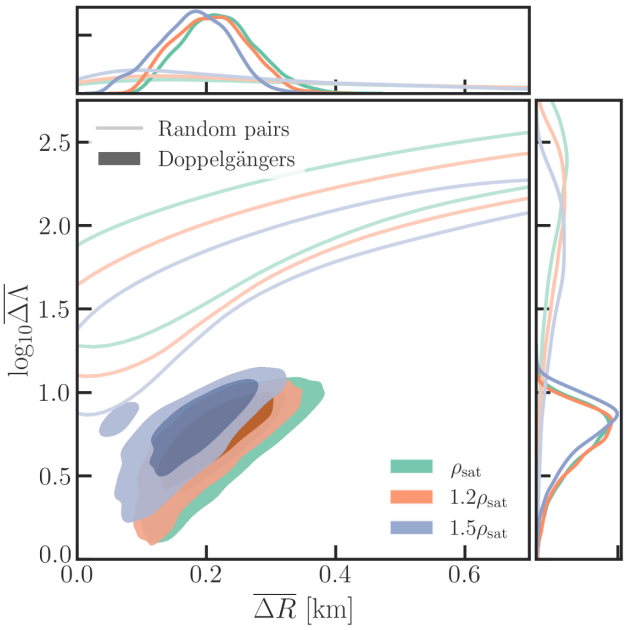

FIG. 3. Contours showing the mass-averaged differences in radius and tidal deformability, calculated across the mass range of 1.17–$2.01M_\odot$. The filled contours show the average differences for the highest-scoring set of doppelgänger EoSs (68% and 95% intervals), while the unfilled contours represent the average differences for pairs of randomly-selected EoSs from each sample (68% intervals). We include results for three EoS samples, for which the PWP parametrization starts at $\rho_0 = \{1, 1.2, \text{ and } 1.5\}\rho_{\rm sat}$, where $\rho_{\rm sat}$ is the nuclear saturation density. All samples use the same crust EoS (ap3) at lower densities and adopt the same weak ($\lambda = 8$) prior on the pressure derivatives at higher densities. As the crust EoS is assumed to higher densities, the allowed doppelgängers become less extreme.

Figure 4 shows the impact of assuming a different crust EoS on the resulting sample of doppelgängers. In this figure, the baseline EoS sample, which assumes ap3 to $\rho_0 = \rho_{\rm sat}$, is repeated in teal for reference. The new EoS sample (shown in yellow) is otherwise identical (i.e., using $\rho_0 = \rho_{\rm sat}$ and the weak prior), but the low-density EoS is exchanged for the stiffer model ms1b. We find that adopting a stiffer crust EoS results in less extreme doppelgängers, characterized by smaller average differences in radii.

Figure 5 likewise shows the impact of modifying the baseline EoS sample (in teal) to use a stronger prior on the

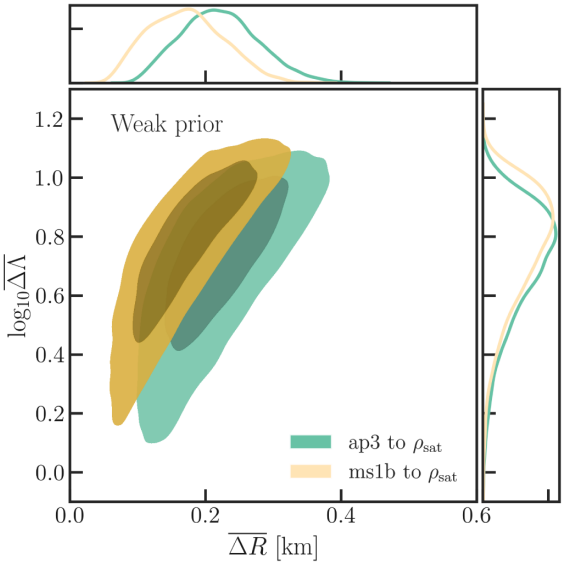

FIG. 4. Same as Fig. 3, but showing the impact of the crust EoS on the doppelgänger populations. Both samples have a fiducial density of $\rho_0 = \rho_{\rm sat}$ and a weak prior on the second derivatives of the pressure. The baseline case using ap3 for the crust EoS is repeated from Fig. 3 in teal; the sample using ms1b for the crust is shown in yellow.

second logarithmic derivative of the pressure (in pink), such that $\lambda = 2$ in Eq. (1). By restricting rapid variations in the pressure as a function of density, the extremity of the doppelgänger models can be further reduced.

To understand these differences as a function of mass, Fig. 6 shows contours of the differences in Λ and R at fixed masses, for each set of doppelgängers identified in Fig. 3. In general, we find that the doppelgängers selected for by Eq. (2) have the largest differences in radius at low masses ($1.2M_\odot$). At all four masses considered, the doppelgängers differ in Λ by a similar degree, albeit with somewhat larger characteristic differences reached at $1.8M_\odot$. In fact, we can see that for this mass, $\Delta\Lambda$ is more strongly correlated with ΔR, whereas $\Delta\Lambda$ is almost independent of ΔR at lower masses. Figure 6 again highlights that assuming the crust EoS to higher densities reduces the parameter space of the doppelgänger EoSs. For example, when the crust EoS is assumed only up to $\rho_{\rm sat}$, the doppelgängers are characterized by $\Delta R_{1.4} \lesssim 0.25$ km. However, in the more restrictive case that the EoS is known to $1.5\rho_{\rm sat}$, the resulting set of most extreme doppelgängers have $\Delta R_{1.4} \lesssim 0.1$ km.

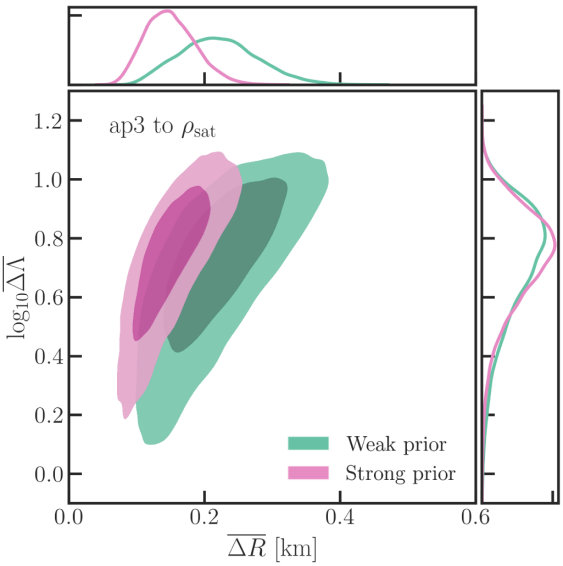

FIG. 5. Same as Fig. 3, but showing the impact of the choice of prior on the doppelgänger populations. Both samples have a fiducial density of $\rho_0 = \rho_{\rm sat}$ and assume ap3 for the crust EoS. The baseline case for a weak prior ($\lambda = 8$) is repeated from Fig. 3 in teal; the sample with a stronger prior ($\lambda = 2$) is shown in pink.

In summary, for all EoS samples considered, we find populations of doppelgänger EoS models that have average differences in the tidal deformability of $\lesssim$10, but that differ in radii by up to a few hundred meters. The extremity of the doppelgänger behavior—characterized by the average differences in radii—can be reduced by enforcing the crust EoS to higher densities, using a crust EoS that is relatively stiff, or by adopting stronger priors on the density derivatives of the pressure.

D. EoS parameter space of the doppelgänger models

We turn now to the EoS parameter space probed by the tidal deformability doppelgängers. Figure 7 illustrates the mass-radius bounds spanned by each population of models from Fig. 3. The lighter shaded regions correspond to the randomly drawn EoSs from the full EoS samples, while the darker shaded regions show the space occupied by the doppelgänger EoSs. We caution that these are merely bounds on the mass-radius space, and that multiple different EoSs may contribute to any given feature along these edges (see e.g., Fig. 3 of [49]). However, these edges already demonstrate clearly that the doppelgänger scoring criterion selects for relatively compact stars.

This is even more apparent when we consider the distributions of radii for stars of fixed mass ($M = 1.4M_\odot$), which are shown in the top panel of Fig. 7. The randomly drawn sample of EoSs peaks strongly towards large $R_{1.4}$, due to the uniform MCMC sampling of the EoSs in pressure space. In spite of this strong preference for large-radius stars in the randomly-drawn EoS sample, the doppelgängers select for more compact neutron stars, with $R_{1.4} \simeq 11$–12 km. As the starting density for the PWP parametrization is increased, the distribution of doppelgängers shifts toward smaller radii and spans a narrower region of the mass-radius plane.

Figure 8 shows the impact on these mass-radius bounds of changing the crust EoS (in yellow) or adopting stronger priors (in pink), compared to the baseline sample of doppelgängers (in teal). For the same starting PWP density of $\rho_0 = \rho_{\rm sat}$, using a stiffer crust EoS such as ms1b causes

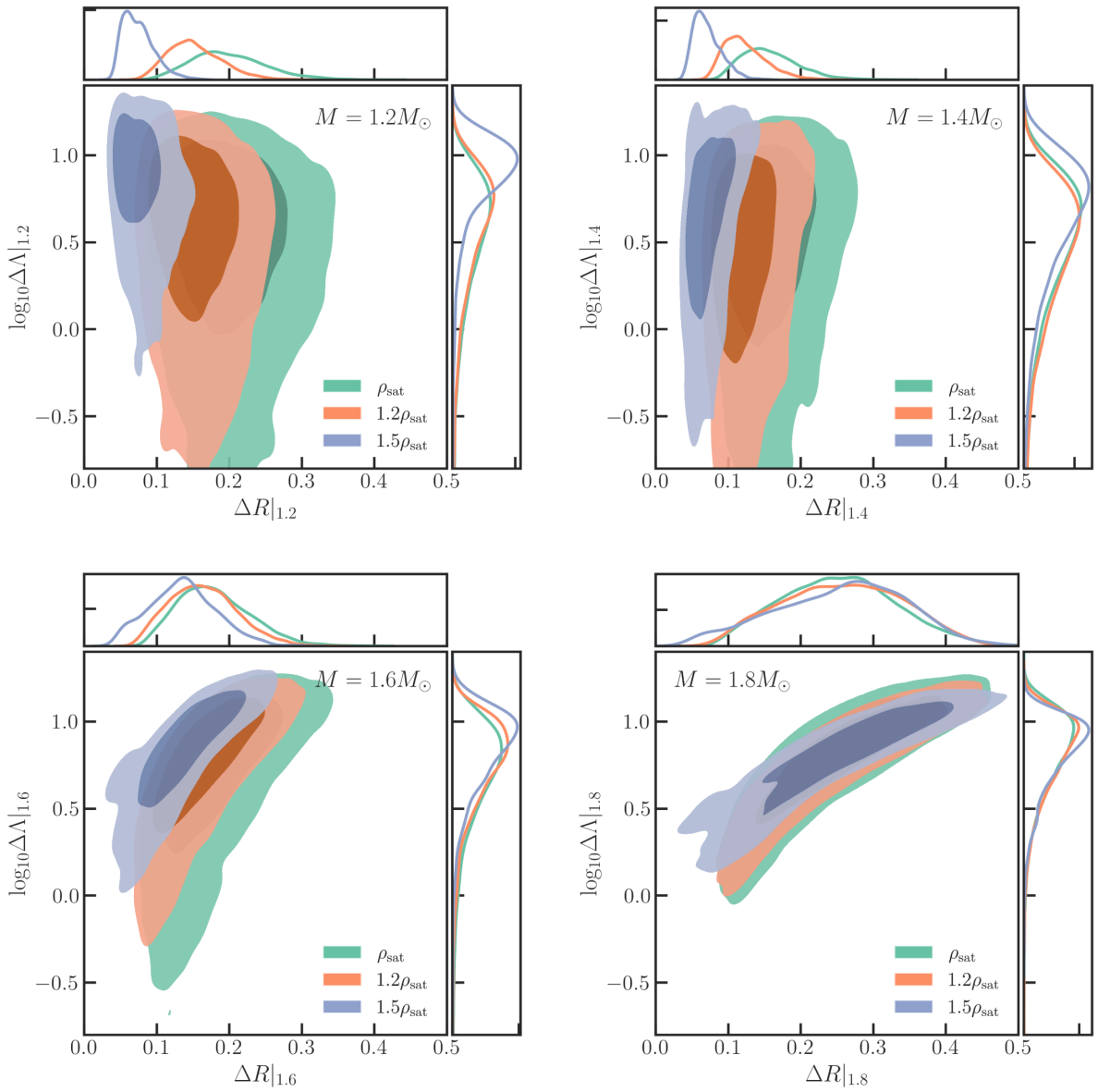

FIG. 6. Contours showing the absolute difference in Λ and R measured at four different masses, for the doppelgängers identified in Fig. 3. The colors indicate the density at which the PWP parametrization begins, below which the crust EoS (ap3) is assumed. All models are sampled with the weak prior. The contours correspond to 68% and 95% intervals. The absolute differences in radii tend to be largest at small masses; while the differences in Λ tend to be largest at higher masses. In all cases, $\Delta\Lambda$ measured at any of these masses is $\lesssim 20$.

the doppelgänger population to shift to larger radii, with the distribution of $R_{1.4}$ peaking at $\sim$12.25 km, compared to $R_{1.4} \sim 11.7$ km for the baseline sample that uses the softer crust EoS ap3. When the stronger prior is adopted, the mass-radius bounds shrink and $R_{1.4}$ is again slightly larger than the weak prior baseline case. The reason for this is that the stronger prior penalizes phase transitions (see Eq. (1)), which generally lead to more compact stars.

For the range of crust EoSs, priors, and starting densities considered here, we find that the doppelgängers occur in a relatively compact region of parameter space. The range of stellar compactness spanned by these models is consistent with current astrophysical constraints from NICER [10–13] and GW170187 [14–16]. However, if future observations find that neutron star radii are significantly larger, it may be possible to constrain the ubiquity and extremity of the doppelgängers by combining nuclear input (e.g., in terms of the densities to which the crust EoS is known) with x-ray observations of neutron stars. We revisit this point in the discussion below.

In order to better understand the parameter space of these models, Figs. 9 and 10 show 2D histograms of the pressure and density for the various populations of doppelgängers. For a given pair of doppelgängers, we identify one EoS as

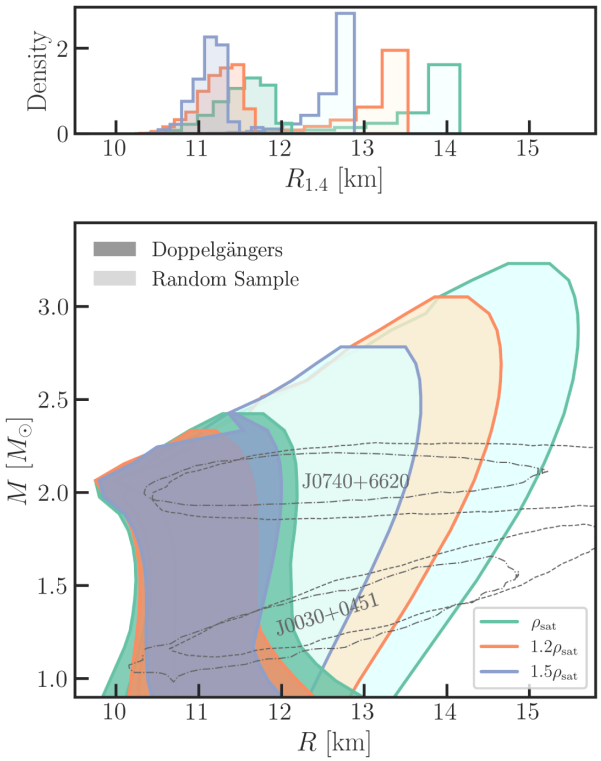

FIG. 7. Mass-radius space spanned by the EoS samples included in Fig. 3. The EoS samples with the PWP parametrization starting from $\rho_{\rm sat}$ are shown in teal, from $1.2\rho_{\rm sat}$ in orange, and from $1.5\rho_{\rm sat}$ in blue. The light-shaded regions show a random sample of 5,000 EoSs, drawn from the complete distribution, while the dark-shaded regions correspond to the sample of highest-scoring doppelgänger EoSs. Mass-radius constraints from NICER are shown in gray dashed [10,12] and dash-dotted lines [11,13]. The corresponding distribution of the radii predicted for a $1.4M_\odot$ neutron star for each of these samples is shown in the top panel. The randomly selected set of EoSs are strongly biased towards large radii, due to the uniform sampling in pressure-density space. In contrast, the doppelgänger criterion selects for more compact stars.

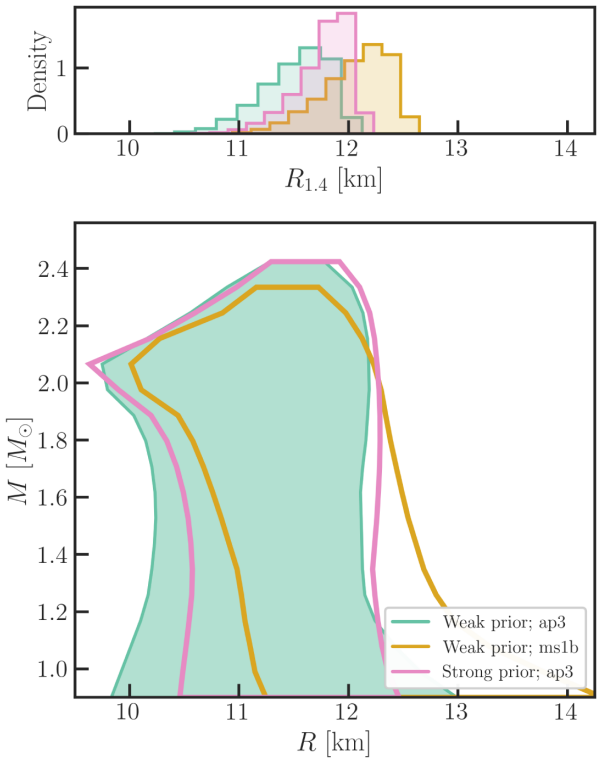

FIG. 8. Same as Fig. 7, but showing the impact of the choice of priors and the crust EoS on the doppelgänger populations, compared to the baseline sample (in teal; repeated from Fig. 7). All samples have a fiducial density of $\rho_0 = \rho_{\rm sat}$. The impact of using the stiffer crust EoS ms1b is shown in yellow. The impact of adopting a stronger prior on the density dependence of the pressure is shown in pink.

"softer" and one as "stiffer", based on which has the larger pressure at the first fiducial density in our parametrization. We then compute the 2D histogram for all of the softer EoSs in blue, and the stiffer EoSs in red. A clear structure emerges in these 2D histograms, with all softer (blue) EoSs exhibiting some degree of a phase transition at densities immediately above ρ_0, for any of the three starting densities considered in Fig. 9. The stiffer (red) EoSs start initially stiff, then soften. We saw a similar behavior in Figs. 1 and 2, where the strongest tidal deformability degeneracy occurred for EoSs that differed maximally in the pressure at low densities, but were similar at higher densities. Here, we see that this signature holds more generally in this larger and randomly generated EoS sample; that is, the doppelgänger degeneracy emerges for EoSs that differ significantly at low densities, with one stiffer EoS rising rapidly in pressure, undergoing a phase transition, and then stiffening again (more slowly) to higher densities. The companion doppelgänger EoS is one that starts with a strong phase transition just above ρ_0, and then stiffens, such that it has the higher pressure just above the first softening of the other EoS.

The large differences between the stiff (red) and soft (blue) doppelgängers in Fig. 9 imply significant differences in the underlying physics of the models. In particular, although the PWP construction is phenomenological in nature, the qualitative features found in Fig. 9 are similar to what is found in more realistic calculations of EoSs with first-order phase transitions to deconfined quark matter, or more generally to the emergence of more exotic degrees of freedom, e.g., [50–52] and references therein. Thus, the degeneracy of the tidal deformability curves for these models suggests some limitation to how well we may be able to resolve phase transitions in some regions of parameter space. We investigate this question in the context of mock EoS inferences from GW data for doppelgänger models in [47].

As the crust EoS is assumed to higher densities, we find in Fig. 9 that the differences in pressures between a given pair of doppelgängers are reduced. For comparison against

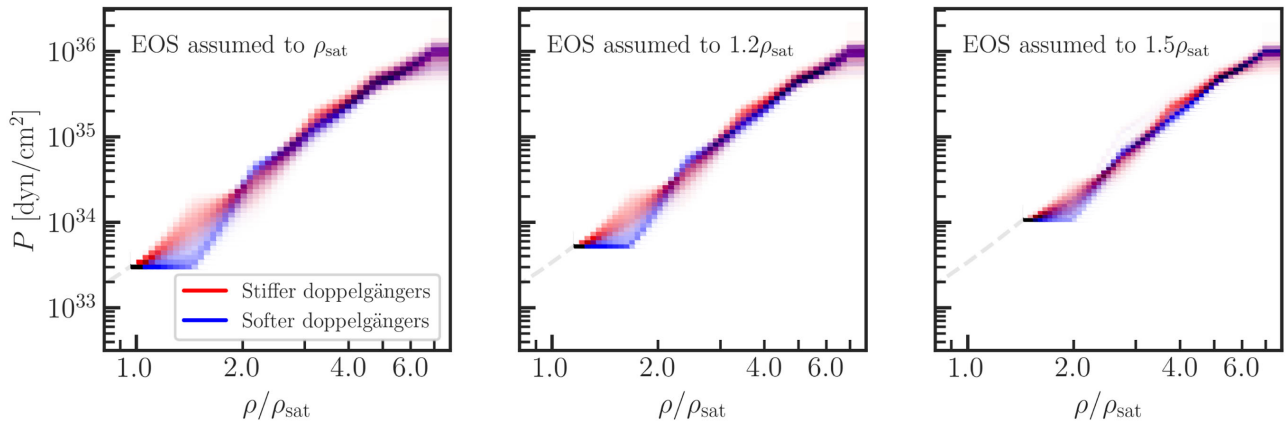

FIG. 9. Pressure-density histograms for the population of doppelgängers identified in Fig. 3. All models use ap3 for the crust EoS and use the weak prior on the density-dependence of the pressure. We classify each EoS in a given pair of doppelgängers as "stiff" or "soft" based on the pressure at the first fiducial density, and we plot the 2D histograms for each subclass in red and blue respectively.

the baseline case (with the PWP parametrization starting at ρ_0), we show also in Fig. 10 the doppelgänger populations with the stronger prior on the pressure derivatives and with the stiffer crust EoS. For the case of the strong prior, which penalizes large second derivatives of the pressure (Eq. (1), first-order phase transitions are severely restricted. Nevertheless, the doppelgänger scoring criteria still selects for EoSs that are maximally different at intermediate densities and selects, when possible, for smoother, crossover phase transitions.

For the crust EoS ms1b in the bottom panel of Fig. 9, we also find smaller differences in the pressures between the stiff and soft doppelgängers, compared to the baseline case which used ap3 for the crust. The reason for this is that ms1b is a relatively stiff EoS (see Fig. 1), thus the parametrization starts from a higher pressure at ρ_0. As a result, there is a narrower region of parameter space in which it is possible to construct a pair of models with the requisite phase transitions to achieve the doppelgänger morphology.

We emphasize that these pressure-density histograms highlight the most extreme pairs of doppelgängers in our full sample. As was shown in Fig. 2, the parameter space between the blue and red curves will also be partially degenerate in tidal deformability. We note that a different parametrization of the EoS (e.g., a constant-sound-speed [53], spectral [54,55] or nonparametric [56,57] representation) may influence the EoS features identified here and the resulting tidal deformability degeneracy as well. Further work will be needed to assess the ubiquity of the doppelgänger degeneracy in other EoS frameworks.

E. I-Love-C quasiuniversal relations

The typical differences of $\lesssim 10$ in the tidal deformability found in Sec. III C are much smaller than expected from the quasiuniversal relation between Λ and the stellar compactness, C, first introduced in [30,58]. This $\Lambda - C$ relation predicts, e.g., that a 0.4 km difference in radii for $R_{1.4} \simeq 12$ km stars should propagate to a difference in $\Lambda_{1.4}$ of 85. More generally, it has been shown that $\Lambda \propto R^{\alpha}$ for a large range of EoSs, where $\alpha \approx 6$ [59–61], which would further imply that small differences in R should propagate to large differences in Λ. Given these standard scaling relations, the small differences in Λ for the doppelgängers are quite surprising.

Curiously, we find that the doppelgänger EoSs still approximately obey the quasiuniversal relations of [30], between not just Λ and C, but also with the dimensionless moment of inertia $\bar{I} \equiv I/M^3$. We show these relations in Fig. 11 for our baseline EoS sample (PWP parametrization starting at $\rho_{\rm sat}$, ap3 for the crust EoS, and a weak prior on the pressure derivatives). The highest-scoring sample of doppelgängers are shown in teal, while the sample of randomly-drawn EoSs are shown in orange. The bottom panel shows the residuals compared to the fit relations from [30].

We find that the doppelgängers obey these standard quasiuniversal relations, with a roughly comparable degree of scatter. In particular, for the $\bar{I} - \Lambda$ relation, which is the tightest relation of the three shown, the doppelgängers obey the existing relation nearly exactly, with errors at the subpercent level. This is nearly indistinguishable from the relation we find for the random sample of EoSs. In the relations between either Λ or $\bar{I}$ and the stellar compactness, which are generally broader, we find that the doppelgängers are approximately consistent with the existing relationships, although there is a systematic deviation from the standard relation at small compactness.

This deviation becomes more evident in Fig. 12, where we show a 2D histogram of the $\Lambda - C$ relation for the same sample of doppelgängers. As in Fig. 9, for each pair of doppelgängers, we identify one softer and one stiffer EoS based on which has the larger pressure at the first fiducial density and we color the resulting histograms in blue and

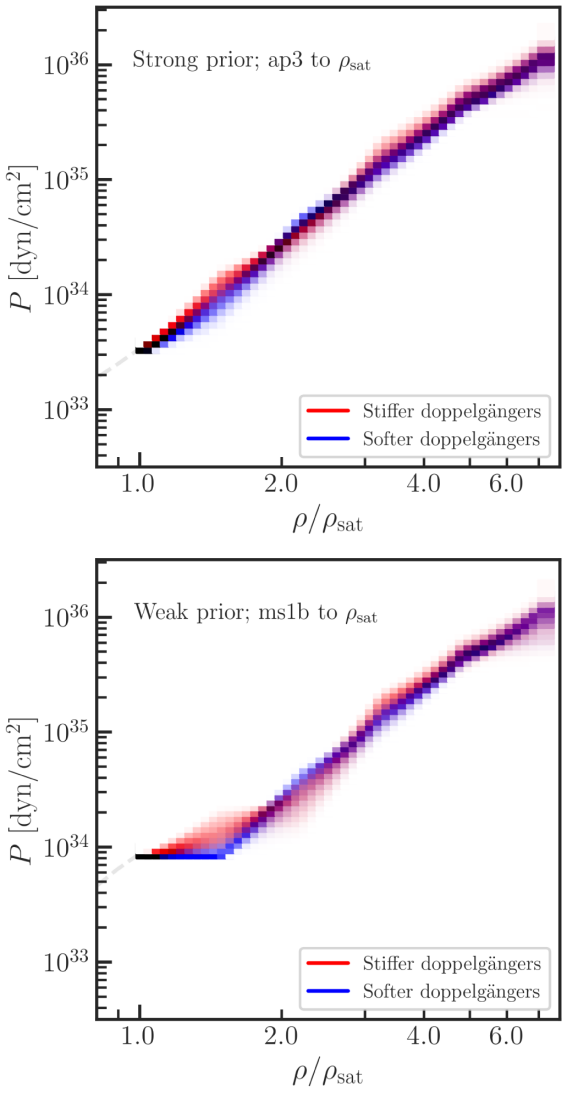

FIG. 10. Same as Fig. 9, but showing the impact of adopting a stronger prior (top) or stiffer crust EoS (bottom) on the population of highest-scoring doppelgängers. The PWP parametrization starts at $\rho_0 = \rho_{\rm sat}$ for all models.

red, respectively. We find that the doppelgänger models tend to fall systematically below the $\Lambda - C$ relationship of [30], with larger deviations at small C. This is perhaps not surprising, given with the compact region of parameter space that these models are found within (see Sec. III D).

We also find that, although the doppelgängers generally obey the standard $\Lambda - C$ relation, they select from distinct regions of this plane, as evidenced by the divide in colors in Fig. 12. That is, the doppelgängers can be interpreted as originating from different subpopulations that exist within the scatter of the broad $\Lambda - C$ relation. The results in Fig. 12 are shown for the weakest set of constraints in order to illustrate the trend.

For completeness, we show the $I - \Lambda - C$ relations for the EoS samples with additional restrictions (in terms of the density to which the crust EoS is assumed, the choice of crust EoS, and the prior) in the Appendix. In all cases, we find that the doppelgängers exhibit a tight $I - \Lambda$ correlation, with subpercent residuals comparable to the relation of [30]. For the $\Lambda - C$ and $I - C$ relations, the doppelgänger models can deviate more significantly from the relations of [30], especially at low C, depending on the restrictions adopted in the EoS sampling.

Finally, we illustrate the origin of the tidal deformability degeneracy in Fig. 13, where we show the tidal Love number, k_2, for one pair of high-scoring doppelgängers (in the top panel), compared to the random population of EoSs (in the bottom panel). We see in this figure that, although the tidal deformabilities of the two doppelgänger EoSs are very similar, their tidal Love numbers differ significantly. Figure 13 additionally shows that for a random sample of EoSs, k_2 is approximately correlated with the neutron star radius. Because the tidal deformability is constructed from these two quantities according to

$$\Lambda = \frac{2}{3} k_2 \left(\frac{R}{M}\right)^5, \tag{3}$$

the bottom panel of Fig. 13 thus also illustrates the known $\Lambda \propto R^\alpha$ scaling relation.

In contrast, the top panel of Fig. 13 shows that the doppelgängers violate this trend between k_2 and the radius, across a limited range of radii. For the doppelgänger models, an increase in k_2 at a given mass is balanced by a decrease in R, and the overall Λ remains approximately unchanged. These results suggest that if a gravitational wave detector were directly sensitive to k_2, the doppelgänger models could be more readily distinguished. However, because the detectors are most sensitive to the product of k_2 and R^5, and because k_2 and R are each sensitive to the EoS at slightly different densities, it is possible to construct models that are approximately degenerate in their tidal deformabilities. We note that these trends hold generally for all of the EoS samples considered, but with differing magnitudes. We show results here for the baseline sample for illustrative effect.

IV. DISCUSSION

The example doppelgängers first constructed by hand in Sec. II and identified generically from samples of randomly-generated EoSs in Sec. III both share a common signature; namely, that the stiffer EoS undergoes some crossover (or, in the more extreme case, first-order) phase transition at supranuclear densities. When compared to a sufficiently soft companion EoS, the resulting models can have nearly identical tidal deformability curves across a wide range of neutron star masses, in spite of significant differences (>100%) in the low-density pressures. We see this behavior in EoS samples that are constructed to obey minimal physical constraints and that are subject to

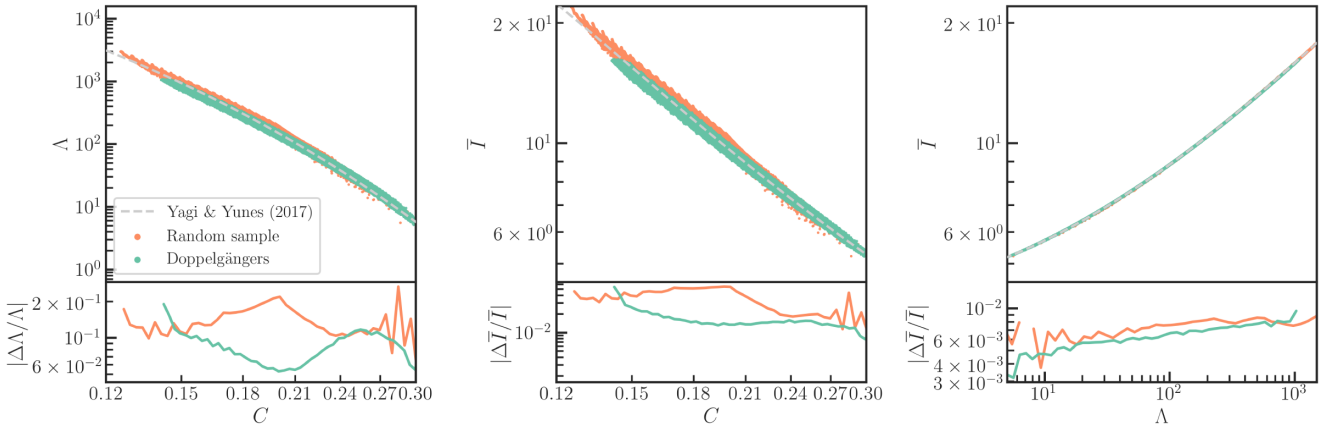

FIG. 11. Quasiuniversal relation between tidal Love number, the neutron star compactness, C, and the dimensionless moment of inertia $\bar{I} \equiv I/M^3$. A random selection of 5000 EoSs from our baseline EoS sample (which assumes the ap3 crust EoS to $\rho_{\rm sat}$ and a weak prior on the pressure derivatives) are shown in orange, while the set of most extreme doppelgängers are shown in teal. The quasiuniversal relations from [62] are shown in gray, dashed lines for reference. The average residuals between the EoS samples and the quasiuniversal fit line are shown in the bottom panels.

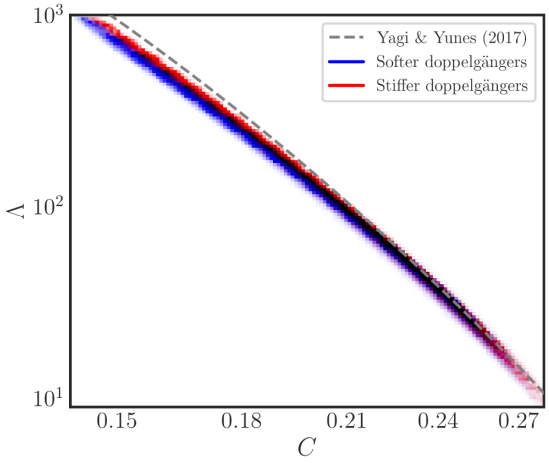

FIG. 12. 2D histogram showing the quasiuniversal relationship between tidal deformability and stellar compactness, for the doppelgängers identified for our baseline EoS sample. We classify each EoS in a given pair of doppelgängers as "stiff" or "soft" based on the pressure at the first fiducial density, and we plot the 2D histograms for each subclass in red and blue respectively. Tidal deformability degeneracy emerges for EoSs that trace out parallel, but offset trends in $\Lambda - C$.

different degrees of nuclear input, in terms of the density to which the crust EoS is utilized and in terms of the prior on the derivatives of the pressure. In every case, we find examples of doppelgänger EoSs, although the extremity of the degeneracy is reduced as more restrictions are added.

The existence of doppelgänger EoSs thus seems to be a natural consequence of allowing for a phase transition. For an EoS to undergo a phase transition and still meet the maximum mass requirement of $\sim 2M_\odot$, it requires a significant degree of stiffening at both lower and higher densities. As we have shown in Fig. 10, one way to reduce the extremity of the allowed doppelgängers is to apply a stronger prior on the second derivative of the pressure. Thus, by folding in constraints on the sound speed in neutron stars from latest astrophysical measurements, combined with theoretical input from chiral EFT [e.g., 63–66], it may be possible to constrain the parameter space of doppelgänger models.

In terms of the crust EoS, further constraints may be possible by incorporating latest results from chiral EFT calculations, which can at least partially constrain the EoS to densities of $2\rho_{\rm sat}$ [67–69], Improvements in low-density experimental constraints will come in the coming years as well, e.g., from measurements of the neutron skin thickness with PREX and CREX [70], new neutron-rich isotope facilities such as FRIB, RIBF, and FAIR, and next-generation heavy-ion colliders such as NICA [71]. As these experiments and theoretical inputs constrain the crust EoS to higher densities, the allowed parameter space for the doppelgänger models will be further reduced.

Another avenue forward is to use the next-generation of astrophysical constraints. Indeed, the most extreme examples of doppelgängers that we constructed predicted neutron star radii that differ by ∼0.5 km (or even 0.7 km, when allowing for further freedom in the crust EoS, as in Sec. II). This is comparable to the anticipated radius accuracy for the brightest NICER targets [72]. Gravitational wave detections of mergers with very low-mass neutron stars ($\sim$1–1.2$M_\odot$) may also help to distinguish between some classes of doppelgängers, as low-mass stars have generally larger differences in tidal deformabilities. If such low-mass systems exist, they may be a prime target for partially resolving the tidal deformability degeneracy directly with GW data. We demonstrate this prospect in the context of an EoS inference from current and upcoming GW data for a pair of doppelgänger models in [47]. However, we note that

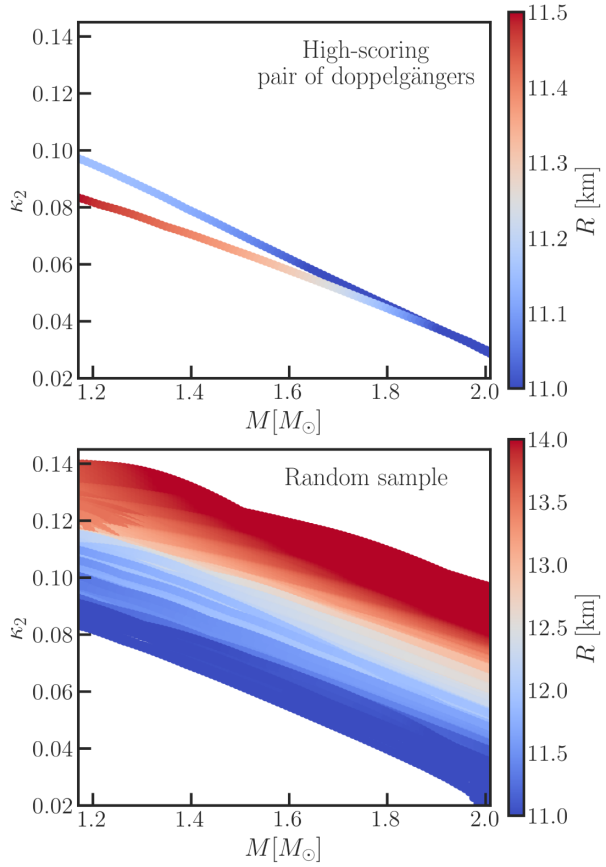

FIG. 13. Tidal Love number as a function of the neutron star mass and radius (shown via the color). The top panel shows these values for one of the highest-scoring examples of doppelgängers, while the bottom panel shows the correlations for a randomly drawn sample of EoSs. All results are shown for the baseline sample, which uses ap3 for the crust EoS up to $\rho_{\rm sat}$, together with the weak prior on the pressure derivatives.

measuring the difference in Λ for such systems will likely still require very high SNRs, at which point current waveform models become prone to systematic errors [29]. Improvements in numerical waveform models are thus crucially needed as well.

Rather than treating each of these types of constraints separately, the most promising route forward will likely be to combine these inputs. For example, consider a scenario in which nuclear theory constrains the crust EoS sufficiently tightly that the allowed parameter space of doppelgängers is restricted to $R_{1.4} \in (10, 12)$ km (as in e.g., Fig. 7). If NICER measures the radius of a future source with high precision to $R_{1.4} > 12$ km or if LIGO likewise measures an incompatible tidal deformability, then the most extreme sets of doppelgängers can effectively be ruled out.

In a companion work to this paper [47], we performed a set of numerical relativity simulations of neutron star mergers, using two example pairs of doppelgänger EoSs. In that work, we investigated the emission of gravitational waves from the postmerger remnant, and found that the peak frequency of the postmerger signal is the same for a given pair of doppelgängers, to within our estimate of the numerical error of the simulations. In other words, it seems that postmerger GWs may not be able to distinguish between doppelgängers either, although this conclusion is subject to the numerical and physical uncertainties of current state-of-the-art simulations, including the possible impact of incorporating more realistic magnetic fields [73–75], more advanced neutrino physics [76–79], finite-temperature effects [80–82], and rapid neutron star spins [83–87], which will need to be considered before a final conclusion can be drawn.

V. SUMMARY AND CONCLUSIONS

In this paper, we have introduced a new class of EoS models that can differ significantly in the pressure near saturation densities and, accordingly, in the radii by up to 0.5 km, but that are surprisingly similar in tidal deformability across the entire range of neutron star masses. These tidal deformability doppelgängers will be challenging to differentiate with the current generation of GW detectors, although next-generation facilities such as Cosmic Explorer or Einstein Telescope may be able to resolve the small differences in Λ for these models.

We have shown that it is not only possible to construct EoSs that have nearly degenerate tidal deformability curves, but that these doppelgängers naturally occur in randomly generated samples of EoS models, as a consequence of allowing for a phase transition at supranuclear densities, where the exact density can be pushed higher by adopting a more restrictive nuclear input. This has important implications for EoS inferences from measurements of the tidal deformability. In particular, even with measurements of tidal deformabilities across a wide range of masses, we have shown that there are some regions of the EoS parameter that will be challenging to distinguish based on the tidal deformabilities alone. This implies a fundamental limit to the level at which the neutron star radius can be constrained from current measurements of the tidal deformability, in the absence of informative nuclear priors that would distinguish between these doppelgänger models.

However, we have also demonstrated that by adopting more restrictive priors on the density dependence of the pressure, or by utilizing the crust EoS to higher densities, that the extremity of the doppelgänger models can be significantly reduced. Thus, by incorporating future constraints from nuclear theory and experiments, x-ray observations of neutron star radii, and population constraints on the tidal deformability from current-generation facilities, it may be possible to significantly constrain the ubiquity of

doppelgänger models, even before the advent of next-generation GW detectors.

ACKNOWLEDGMENTS

The authors thank Gabriele Bozzola, Katerina Chatziioannou, Pierre Christian, Philippe Landry, Feryal Özel, Dimitrios Psaltis, Jocelyn Read, Ingo Tews, and Nicolas Yunes for insightful comments on this work. The authors gratefully acknowledge support from postdoctoral fellowships at the Princeton Center for Theoretical Science, the Princeton Gravity Initiative, and the Institute for Advanced Study. C. A. R. additionally acknowledges support as a John N. Bahcall Fellow at the Institute for Advanced Study. This work was performed in part at the Aspen Center for Physics, which is supported by National Science Foundation Grant No. PHY-1607611. The EoS parameter survey was performed on computational resources managed and supported by Princeton Research Computing, a consortium of groups including the Princeton Institute for Computational Science and Engineering (PICSciE) and the Office of Information Technology's High Performance Computing Center and Visualization Laboratory at Princeton University.

APPENDIX: I-LOVE-C RELATIONS FOR ADDITIONAL EOS SAMPLES

In this appendix, we report the I-Love-C relations for three additional EoS samples, to demonstrate the impact of assuming the crust EoS to a higher density of $\rho_0 = 1.5\rho_{\rm sat}$ (in Fig. 14), using a stonger prior on the high-density pressure derivatives (in Fig. 15), and adopting the stiffer crust EoS ms1b (in Fig. 16). In each of these figures, we show the correlations between tidal deformability, moment of inertia, and compactness for both a set of randomly selected EoSs (in orange) or the highest-scoring set of doppelgängers from a given EoS sample (in teal).

For all three of these EoS samples, which adopt additional restrictions compared to the baseline EoS sample described in Sec. III E, we find that the $I-\Lambda$ relation still holds, almost exactly, for the doppelgänger models. In particular, $I-\Lambda$ correlation for the doppelgänger models matches that of Ref. [30] with subpercent residuals, indistinguishable from the correlation for the randomly selected set of EoS models.

In contrast, we find larger deviations of up to ∼30% in the $\Lambda-C$ and $I-C$ relations for the doppelgänger models, compared to the quasiuniversal relations of [30]. The deviations are largest in the $\Lambda-C$ correlations at small compactness.

Thus, although the EoS samples shown in Figs. 14–16 have more restrictions than the baseline EoS sample of Sec. III E, they deviate more significantly from the existing quasiuniversal $\Lambda-C$ relations. Depending on the region of parameter space in which the true EoS resides, these deviations may bias EoS inferences that incorporate the standard $\Lambda-C$ fits; e.g., as was done in one of the EoS inferences of the LIGO-Virgo anaylsis of GW170817 [16].

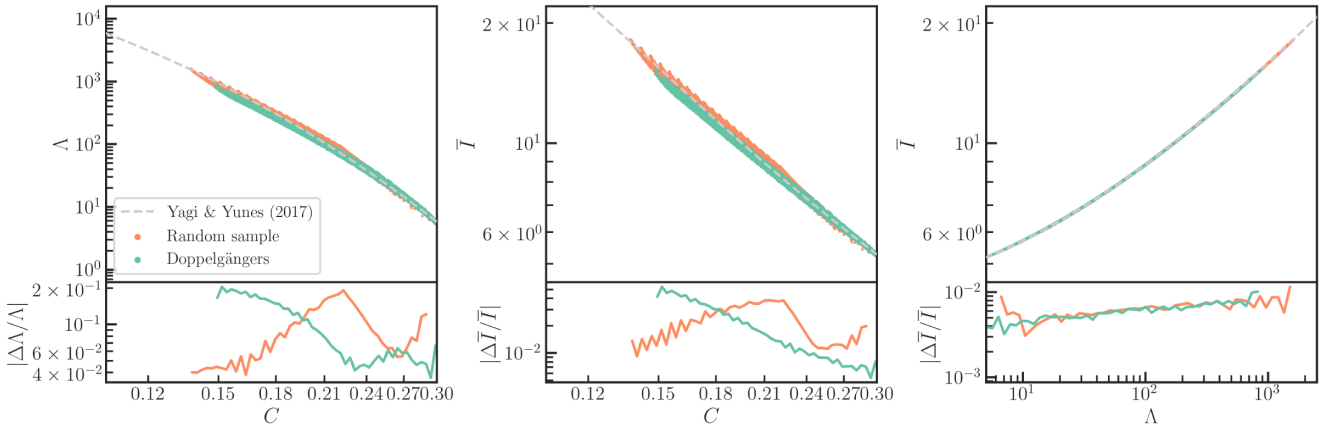

FIG. 14. Same as Fig. 11, but for the EoS sample that assumes the crust EoS ap3 to $\rho_0 = 1.5\rho_{\rm sat}$, with the weak prior. Caption details from Fig. 11 are repeated for convenience: Quasiuniversal relation between tidal Love number, the neutron star compactness, C, and the dimensionless moment of inertia $\bar{I} \equiv I/M^3$. A random selection of 5,000 EoSs from is shown in orange, while the set of doppelgängers is shown in teal. The quasiuniversal relations from [62] are shown in gray, dashed lines for reference. The average residuals between the EoS samples and the quasiuniversal fit line are shown in the bottom panels.

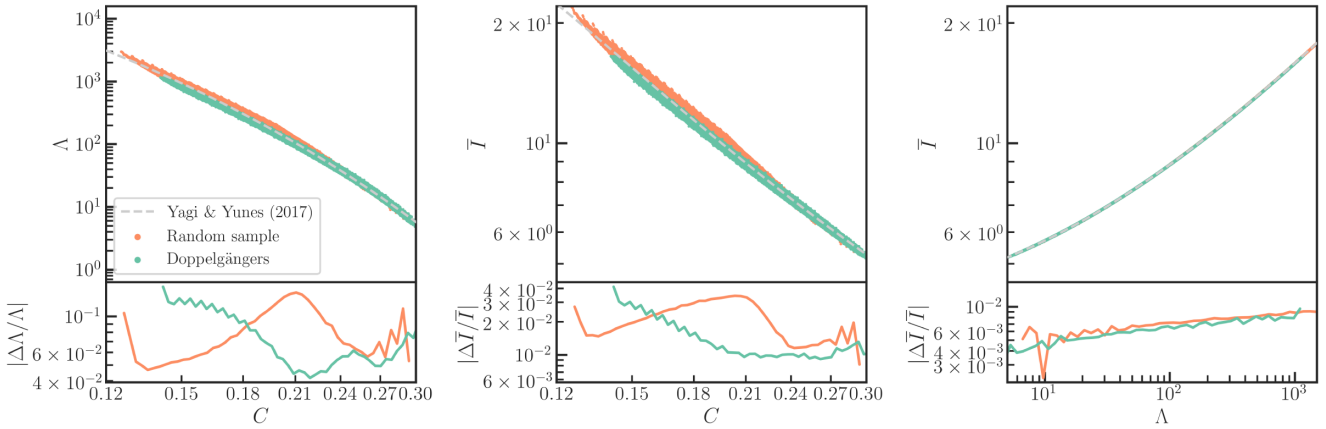

FIG. 15. Same as Fig. 14, but showing the impact of adopting a stronger prior on the pressure derivatives. The EoS samples assume the crust EoS ap3 to $\rho_0 = \rho_{\rm sat}$.

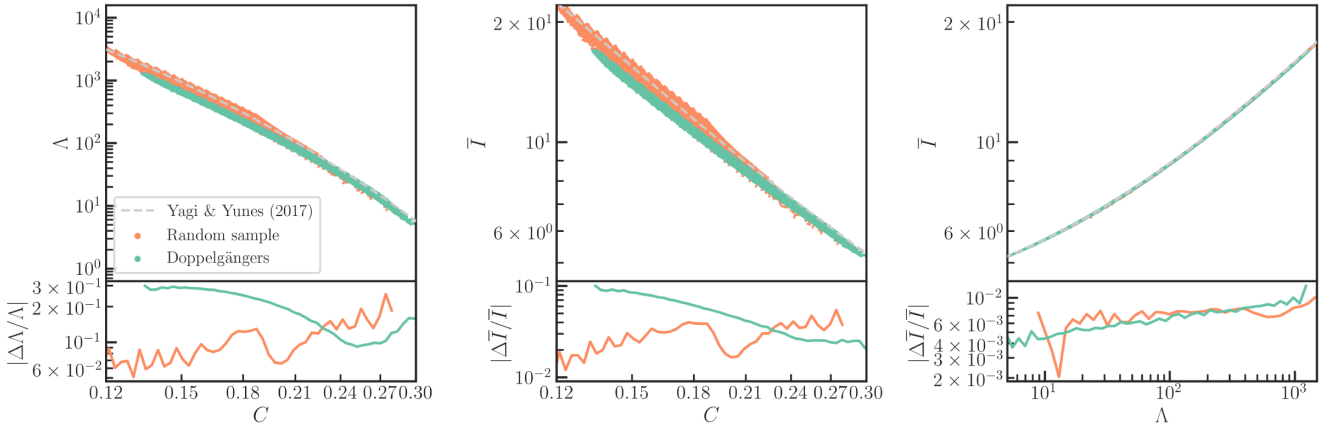

FIG. 16. Same as Fig. 14, but showing the impact of adopting the stiffer crust EoS, ms1b. The EoS samples assume this crust EoS to $\rho_0 = \rho_{\rm sat}$ and adopt a weak prior.

[1] F. Özel, T. Güver, and D. Psaltis, Astrophys. J. **693**, 1775 (2009).
[2] T. Güver, F. Özel, A. Cabrera-Lavers, and P. Wroblewski, Astrophys. J. **712**, 964 (2010).
[3] S. Guillot, M. Servillat, N. A. Webb, and R. E. Rutledge, Astrophys. J. **772**, 7 (2013).
[4] S. Guillot and R. E. Rutledge, Astrophys. J. Lett. **796**, L3 (2014).
[5] C. O. Heinke, H. N. Cohn, P. M. Lugger, N. A. Webb, W. C. G. Ho, J. Anderson, S. Campana, S. Bogdanov, D. Haggard, A. M. Cool *et al.*, Mon. Not. R. Astron. Soc. **444**, 443 (2014).
[6] J. Nättilä, A. W. Steiner, J. J. E. Kajava, V. F. Suleimanov, and J. Poutanen, Astron. Astrophys. **591**, A25 (2016).
[7] F. Özel, D. Psaltis, T. Güver, G. Baym, C. Heinke, and S. Guillot, Astrophys. J. **820**, 28 (2016).
[8] S. Bogdanov, C. O. Heinke, F. Özel, and T. Güver, Astrophys. J. **831**, 184 (2016).
[9] F. Özel and P. Freire, Annu. Rev. Astron. Astrophys. **54**, 401 (2016).
[10] M. C. Miller *et al.*, Astrophys. J. Lett. **887**, L24 (2019).
[11] T. E. Riley *et al.*, Astrophys. J. Lett. **887**, L21 (2019).
[12] M. C. Miller *et al.*, Astrophys. J. Lett. **918**, L28 (2021).
[13] T. E. Riley *et al.*, Astrophys. J. Lett. **918**, L27 (2021).
[14] B. P. Abbott *et al.* (LIGO Scientific and Virgo Collaborations), Phys. Rev. Lett. **119**, 161101 (2017).
[15] B. P. Abbott *et al.* (LIGO Scientific and Virgo Collaborations), Phys. Rev. X **9**, 011001 (2019).

[16] B. P. Abbott *et al.* (LIGO Scientific and Virgo Collaborations), Phys. Rev. Lett. **121**, 161101 (2018).
[17] B. D. Lackey and L. Wade, Phys. Rev. D **91**, 043002 (2015).
[18] R. Essick, P. Landry, and D. E. Holz, Phys. Rev. D **101**, 063007 (2020).
[19] P. Landry, R. Essick, and K. Chatziioannou, Phys. Rev. D **101**, 123007 (2020).
[20] F. Hernandez Vivanco, R. Smith, E. Thrane, and P. D. Lasky, Mon. Not. R. Astron. Soc. **499**, 5972 (2020).
[21] M. M. Forbes, S. Bose, S. Reddy, D. Zhou, A. Mukherjee, and S. De, Phys. Rev. D **100**, 083010 (2019).
[22] D. Reitze *et al.*, Bull. Am. Astron. Soc. **51**, 035 (2019).
[23] M. Punturo *et al.*, Classical Quantum Gravity **27**, 194002 (2010).
[24] K. Ackley *et al.*, Pub. Astron. Soc. Aust. **37**, e047 (2020).
[25] Z. Carson, K. Chatziioannou, C.-J. Haster, K. Yagi, and N. Yunes, Phys. Rev. D **99**, 083016 (2019).
[26] K. Chatziioannou, Phys. Rev. D **105**, 084021 (2022).
[27] G. Pratten, P. Schmidt, and N. Williams, Phys. Rev. Lett. **129**, 081102 (2022).
[28] R. Gamba and S. Bernuzzi, Phys. Rev. D **107**, 044014 (2023).
[29] R. Gamba, M. Breschi, S. Bernuzzi, M. Agathos, and A. Nagar, Phys. Rev. D **103**, 124015 (2021).
[30] K. Yagi and N. Yunes, Phys. Rep. **681**, 1 (2017).
[31] A. Gezerlis, I. Tews, E. Epelbaum, S. Gandolfi, K. Hebeler, A. Nogga, and A. Schwenk, Phys. Rev. Lett. **111**, 032501 (2013).
[32] J. E. Lynn, I. Tews, J. Carlson, S. Gandolfi, A. Gezerlis, K. E. Schmidt, and A. Schwenk, Phys. Rev. Lett. **116**, 062501 (2016).
[33] I. Tews, S. Gandolfi, A. Gezerlis, and A. Schwenk, Phys. Rev. C **93**, 024305 (2016).
[34] C. Drischler, K. Hebeler, and A. Schwenk, Phys. Rev. Lett. **122**, 042501 (2019).
[35] J. S. Read, B. D. Lackey, B. J. Owen, and J. L. Friedman, Phys. Rev. D **79**, 124032 (2009).
[36] F. Özel and D. Psaltis, Phys. Rev. D **80**, 103003 (2009).
[37] C. A. Raithel, F. Ozel, and D. Psaltis, Astrophys. J. **831**, 44 (2016).
[38] H. T. Cromartie *et al.* (NANOGrav Collaboration), Nat. Astron. **4**, 72 (2019).
[39] E. Fonseca *et al.*, Astrophys. J. Lett. **915**, L12 (2021).
[40] A. Akmal, V. R. Pandharipande, and D. G. Ravenhall, Phys. Rev. C **58**, 1804 (1998).
[41] H. Mueller and B. D. Serot, Nucl. Phys. **A606**, 508 (1996).
[42] N. K. Glendenning, Astrophys. J. **293**, 470 (1985).
[43] M. Alford, M. Braby, M. W. Paris, and S. Reddy, Astrophys. J. **629**, 969 (2005).
[44] R. B. Wiringa, V. Fiks, and A. Fabrocini, Phys. Rev. C **38**, 1010 (1988).
[45] J. S. Read, B. D. Lackey, B. J. Owen, and J. L. Friedman, Phys. Rev. D **79**, 124032 (2009).
[46] J. G. Martinez, K. Stovall, P. C. C. Freire, J. S. Deneva, F. A. Jenet, M. A. McLaughlin, M. Bagchi, S. D. Bates, and A. Ridolfi, Astrophys. J. **812**, 143 (2015).
[47] C. A. Raithel and E. R. Most, Phys. Rev. Lett. **130**, 201403 (2023).
[48] R. Gamba, J. S. Read, and L. E. Wade, Classical Quantum Gravity **37**, 025008 (2020).
[49] C. A. Raithel, F. Özel, and D. Psaltis, Astrophys. J. **844**, 156 (2017).
[50] T. Kojo, P. D. Powell, Y. Song, and G. Baym, Phys. Rev. D **91**, 045003 (2015).
[51] G. Baym, T. Hatsuda, T. Kojo, P. D. Powell, Y. Song, and T. Takatsuka, Rep. Prog. Phys. **81**, 056902 (2018).
[52] D. Blaschke and N. Chamel, Astrophysics and Space Science Library **457**, 337 (2018).
[53] E. Annala, T. Gorda, A. Kurkela, J. Nättilä, and A. Vuorinen, Nat. Phys. **16**, 907 (2020).
[54] L. Lindblom, Phys. Rev. D **97**, 123019 (2018).
[55] L. Lindblom, Phys. Rev. D **105**, 063031 (2022).
[56] P. Landry and R. Essick, Phys. Rev. D **99**, 084049 (2019).
[57] I. Legred, K. Chatziioannou, R. Essick, and P. Landry, Phys. Rev. D **105**, 043016 (2022).
[58] K. Yagi and N. Yunes, Phys. Rev. D **88**, 023009 (2013).
[59] S. De, D. Finstad, J. M. Lattimer, D. A. Brown, E. Berger, and C. M. Biwer, Phys. Rev. Lett. **121**, 091102 (2018); **121**, 259902(E) (2018).
[60] C. Raithel, F. Özel, and D. Psaltis, Astrophys. J. Lett. **857**, L23 (2018).
[61] T. Zhao and J. M. Lattimer, Phys. Rev. D **98**, 063020 (2018).
[62] K. Yagi and N. Yunes, Phys. Rep. **681**, 1 (2017).
[63] I. Tews, J. Carlson, S. Gandolfi, and S. Reddy, Astrophys. J. **860**, 149 (2018).
[64] B. Reed and C. J. Horowitz, Phys. Rev. C **101**, 045803 (2020).
[65] C. Drischler, S. Han, and S. Reddy, Phys. Rev. C **105**, 035808 (2022).
[66] S. Altiparmak, C. Ecker, and L. Rezzolla, Astrophys. J. Lett. **939**, L34 (2022).
[67] K. Hebeler, J. D. Holt, J. Menendez, and A. Schwenk, Annu. Rev. Nucl. Part. Sci. **65**, 457 (2015).
[68] J. E. Lynn, I. Tews, S. Gandolfi, and A. Lovato, Annu. Rev. Nucl. Part. Sci. **69**, 279 (2019).
[69] C. Drischler, J. W. Holt, and C. Wellenhofer, Annu. Rev. Nucl. Part. Sci. **71**, 403 (2021).
[70] M. Thiel, C. Sfienti, J. Piekarewicz, C. J. Horowitz, and M. Vanderhaeghen, J. Phys. G **46**, 093003 (2019).
[71] H. Schatz *et al.*, J. Phys. G **49**, 110502 (2022).
[72] K. C. Gendreau, Z. Arzoumanian, and T. Okajima, in *Space Telescopes and Instrumentation 2012: Ultraviolet to Gamma Ray*, edited by T. Takahashi, S. S. Murray, and J.-W. A. den Herder, Society of Photo-Optical Instrumentation Engineers (SPIE) Conference Series Vol. 8443 (SPIE, Bellingham, Washington, 2012), p. 844313.
[73] K. Kiuchi, P. Cerdá-Durán, K. Kyutoku, Y. Sekiguchi, and M. Shibata, Phys. Rev. D **92**, 124034 (2015).
[74] K. Kiuchi, K. Kyutoku, Y. Sekiguchi, and M. Shibata, Phys. Rev. D **97**, 124039 (2018).
[75] C. Palenzuela, R. Aguilera-Miret, F. Carrasco, R. Ciolfi, J. V. Kalinani, W. Kastaun, B. Miñano, and D. Viganò, Phys. Rev. D **106**, 023013 (2022).
[76] M. G. Alford, L. Bovard, M. Hanauske, L. Rezzolla, and K. Schwenzer, Phys. Rev. Lett. **120**, 041101 (2018).

[77] E. R. Most, S. P. Harris, C. Plumberg, M. G. Alford, J. Noronha, J. Noronha-Hostler, F. Pretorius, H. Witek, and N. Yunes, Mon. Not. R. Astron. Soc. **509**, 1096 (2021).
[78] D. Radice, S. Bernuzzi, A. Perego, and R. Haas, Mon. Not. R. Astron. Soc. **512**, 1499 (2022).
[79] E. R. Most, A. Haber, S. P. Harris, Z. Zhang, M. G. Alford, and J. Noronha, arXiv:2207.00442.
[80] A. Bauswein, H. T. Janka, and R. Oechslin, Phys. Rev. D **82**, 084043 (2010).
[81] A. Figura, J. J. Lu, G. F. Burgio, Z. H. Li, and H. J. Schulze, Phys. Rev. D **102**, 043006 (2020).
[82] C. Raithel, V. Paschalidis, and F. Özel, Phys. Rev. D **104**, 063016 (2021).
[83] T. Dietrich, S. Bernuzzi, M. Ujevic, and W. Tichy, Phys. Rev. D **95**, 044045 (2017).
[84] W. E. East, V. Paschalidis, F. Pretorius, and A. Tsokaros, Phys. Rev. D **100**, 124042 (2019).
[85] E. R. Most, L. J. Papenfort, A. Tsokaros, and L. Rezzolla, Astrophys. J. **884**, 40 (2019).
[86] A. Tsokaros, M. Ruiz, and S. L. Shapiro, Astrophys. J. **905**, 48 (2020).
[87] L. J. Papenfort, E. R. Most, S. Tootle, and L. Rezzolla, Mon. Not. R. Astron. Soc. **513**, 3646 (2022).